

Research Article www.acsami.org

# Understanding the Copassivation Effect of CI and Se for CdTe Grain **Boundaries**

Akash Shah,\* Anthony P. Nicholson, Thomas A. M. Fiducia, Ali Abbas, Ramesh Pandey, Junliang Liu, Chris Grovenor, John M. Walls, Walajabad S. Sampath, and Amit H. Munshi



**Cite This:** ACS Appl. Mater. Interfaces 2021, 13, 35086–35096



**ACCESS** III Metrics & More Article Recommendations CdTe/No CdCl<sub>2</sub> Current density (mA/cm²) CdTe/CdCl<sub>2</sub> CdSexTe1-x/CdTe/CdCl2 20 10

-10 -20 0.5

ABSTRACT: Chlorine passivation treatment of cadmium telluride (CdTe) solar cells improves device performance by assisting electron-hole carrier separation at CdTe grain boundaries. Further improvement in device efficiency is observed after alloying the CdTe absorber layer with selenium. High-resolution secondary ion mass spectroscopy (NanoSIMS) imaging has been used to determine the distribution of selenium and chlorine at the CdTe grain boundaries in a selenium-graded CdTe device. Atomistic modeling based on density functional theory (DFT-1/2) further reveals that the presence of selenium and chlorine at an exemplar (110)/(100) CdTe grain boundary passivates critical acceptor defects and leads to n-type inversion at the grain boundary. The defect state analysis provides an explanation for the band-bending effects observed in the energy band alignment results, thereby elucidating mechanisms for high efficiencies observed in Se-alloyed and Cl-passivated CdTe solar cells.

KEYWORDS: CdTe solar cells, atomistic modeling, defect passivation, grain boundaries, energy band alignment, density functional theory, electronic structure

#### INTRODUCTION

Cadmium telluride solar cells are a key technology in the photovoltaic (PV) market. The optimization of processing steps such as alloying selenium (Se) with the CdTe and replacement of contact and buffer layers has led to a 22.1% efficient researchscale CdTe device. 1-4 One of the important fabrication steps that have enhanced efficiency involves cadmium chloride (CdCl<sub>2</sub>) treatment of the CdTe absorber layer. The published literature shows that the CdCl<sub>2</sub> treatment of polycrystalline (px) CdTe-based cells leads to superior device performance compared to single-crystal CdTe-based solar cells.<sup>5</sup> This suggests that the chlorine (Cl) interaction with the grain boundaries is crucial to obtain high efficiencies in px-CdTe solar cells.

Over the years, researchers have proposed several mechanisms to explain the success of CdCl<sub>2</sub> treatment in improving the CdTe device performance.<sup>6</sup> Numerous reports conclude that the high-temperature CdCl<sub>2</sub> treatment of the CdTe layer leads to recrystallization and grain growth along the close-packed

(111) orientation. <sup>7–9</sup> It has also been proposed that CdCl<sub>2</sub> heat treatment passivates the deep defect levels and enhances the charge carrier lifetime. 6,10,11 In another report, Li et al. using scanning transmission electron microscopy along with density functional theory (DFT) described that Cl substitution of the tellurium (Te) sites leads to n-type inversion at the grain boundary.<sup>12</sup> Therefore, a local p-n junction is established between the grain interior and the grain boundary which assists in separation of electron-hole pair charge carriers.

Along with CdCl<sub>2</sub> passivation treatment, recent device efficiency improvements to 22.1% have been realized by alloying

Received: April 11, 2021 Accepted: July 1, 2021 Published: July 15, 2021





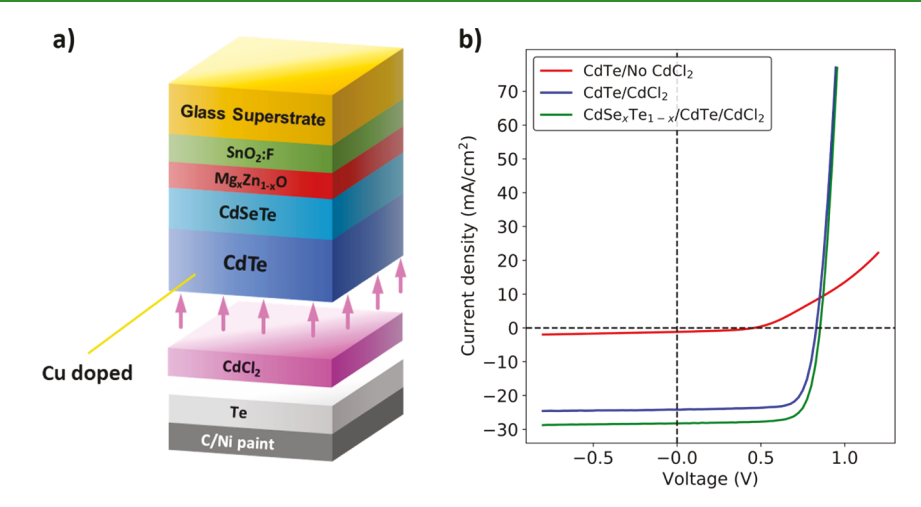


Figure 1. (a) Schematic showing a highly efficient CdSeTe/CdTe PV device in a superstrate configuration (not to scale). (b) Comparison of the best-performing untreated CdTe, CdCl<sub>2</sub>-treated CdTe, and CdCl<sub>2</sub>-treated CdSeTe/CdTe PV devices.

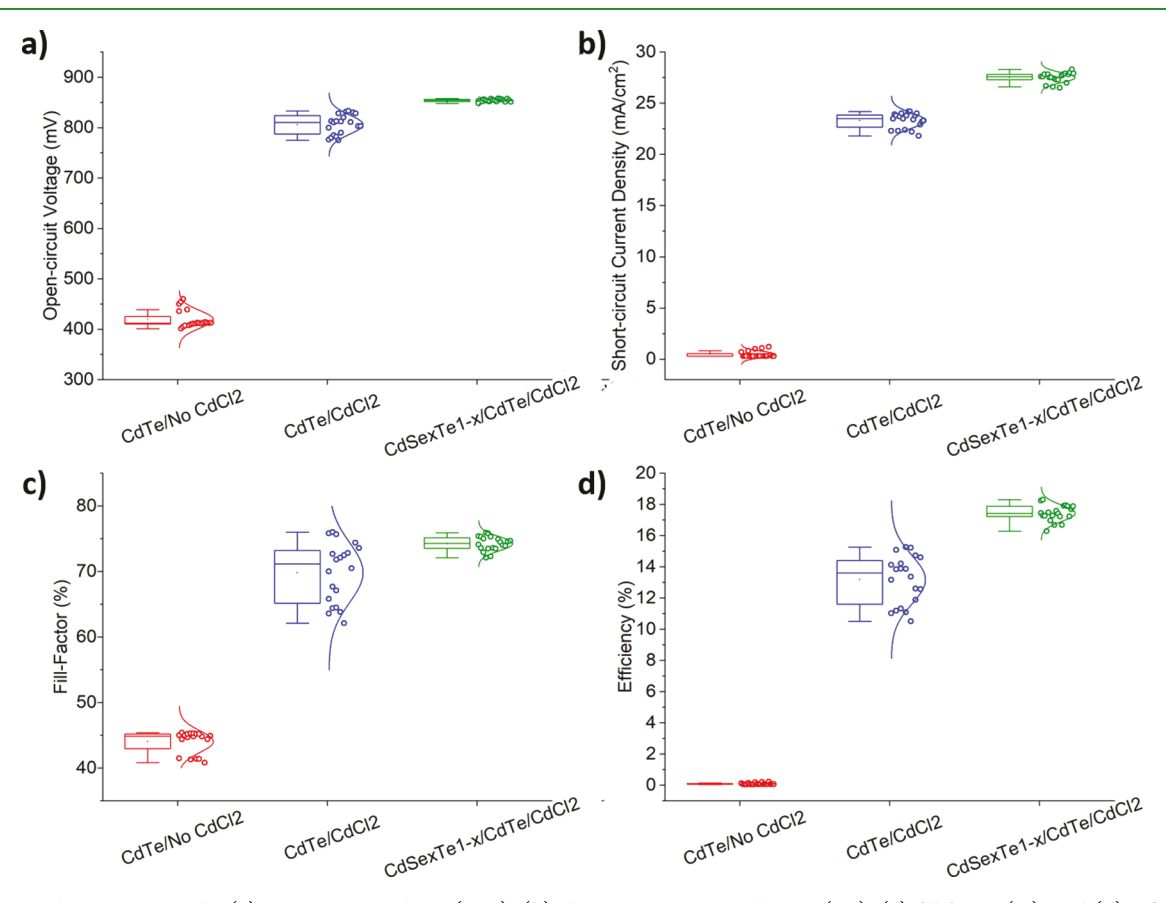


Figure 2. Box plot comparing the (a) open-circuit voltage ( $V_{\rm OC}$ ), (b) short-circuit current density ( $J_{\rm SC}$ ), (c) fill factor (%), and (d) efficiency ( $\eta$ ) between untreated CdTe, CdCl<sub>2</sub>-treated CdTe, and CdCl<sub>2</sub>-treated CdSeTe/CdTe PV devices. Each box plot contains device data for 20 solar cells.

Se within the CdTe film. The published literature reveals that  $CdCl_2$  treatment of the Se-alloyed CdTe layer leads to Se grading through the CdTe grain boundary, forming a graded  $CdSe_xTe_{1-x}/CdTe$  absorber layer. One study shows that grading Se in the CdTe film passivates the nonradiative recombination centers in the bulk material. It is also thought that the improvement in minority carrier lifetime is due to the presence of Se and Cl in the CdTe grain boundaries. These findings emphasize the need to understand the effects of grading Se from  $CdSe_xTe_{1-x}$  to CdTe absorber layers to further improve the device performance.

Several studies in the past using experimental and theoretical techniques have explored the electronic properties of bulk  $CdSe_xTe_{1-x}$ . However, the combined effects of Se and Cl at the CdTe grain boundaries on the electronic structure and charge carrier transport behaviors are unknown. In this work, we report the Se and Cl atomic scale composition and electronic structure of the grain boundaries through NanoSIMS and DFT simulations, respectively. The study demonstrates that alloying Se and Cl together at the grain boundary passivates deep level acceptor trap states when compared to bare (unalloyed) or only Cl at the CdTe grain boundary. The energy band alignment

result shows high density of benign donor states existing below the Fermi level. The presence of high-density benign donor states inverts the boundary region from p-type to n-type, establishing a local p-n junction for efficient charge extraction. This understanding of the role of Se and Cl in copassivating the CdTe grain boundary defect states provides useful details that can further contribute to higher CdTe device efficiency.

#### RESULTS

CdTe and CdSe, Te1-x/CdTe Absorber-Based PV Devices. To perform the study, two CdTe cells (with and without Cl) and one CdSeTe/CdTe absorber-based solar cell were fabricated as described in the Methods section. Figure 1a shows the schematic device structure of the CdSeTe/CdTe solar cell. To understand the effect of alloying selenium and chlorine on the device performance, the CdSeTe/CdTe film and one CdTe absorber-based substrate received the CdCl<sub>2</sub> treatment while the other CdTe substrate was furnished into a device without any CdCl<sub>2</sub> treatment. The electrical measurements were performed on the finished devices to generate the current density versus voltage diode curves. The box plot (see Figure 2) depicts the open-circuit voltage  $(V_{\rm OC})$ , short-circuit current density  $(J_{\rm SC})$ , fill factor (%), and efficiency ( $\eta$ ) comparison between the untreated CdTe, CdCl2-treated CdTe, and CdCl2-treated CdSeTe/CdTe-based PV devices. Comparing the device parameters from the box plot results (see Figure 2), it was evident that the CdCl<sub>2</sub> treatment of the CdTe absorber layer plays a prominent role in bolstering the PV device performance from <1 to 15% + efficiency.

For CdCl<sub>2</sub>-treated CdSeTe/CdTe absorber-based solar cells, a notable increase in  $J_{SC}$  was obtained due to the use of a smaller band gap CdSeTe material toward the front of the device. The small band gap absorber material increases light absorption in the longer wavelength region of the spectrum and thus more current can be extracted from the PV device. 1,13 In addition to an improved short-circuit current, alloying Se in the CdTe layer also enhances the open-circuit voltage values in CdSeTe/CdTe PV devices (Figure 2a). Such an improvement in the  $V_{\rm OC}$  values has been credited to improved minority carrier lifetimes in the absorber. 1,13,19 Figure 1b shows the current density-voltage diode curves for the best-performing devices from each substrate. The best-performing untreated CdTe device gave an efficiency of 0.22%, while the CdCl2-treated CdTe device gave an efficiency of 15.27%. The efficiency value further increased to 18.30% for the CdCl<sub>2</sub>-treated CdSeTe/CdTe PV device. Table 1 summarizes the measured device parameters for the above mentioned three best-performing devices.

To understand the atomic distribution of Se and Cl atoms in the highly efficient CdCl<sub>2</sub>-treated CdSeTe/CdTe PV device, the elemental mapping was performed using the NanoSIMS technique (described in the Methods section) on a similar CdCl<sub>2</sub>-treated CdSeTe/CdTe absorber film. Figure 3a shows a plane-view image of the chlorine signal intensity in the Se-

Table 1. J-V Measurement Comparison of the Best-Performing CdTe/no CdCl<sub>2</sub>, CdTe/CdCl<sub>2</sub>, and CdSe<sub>x</sub>Te<sub>1-x</sub>/ CdTe/CdCl<sub>2</sub> PV Devices

absorber layer	$J_{SC}$ (mA/cm <sup>2</sup> )	$V_{\rm OC}~({\rm mV})$	% FF	% η	
CdTe/no CdCl <sub>2</sub>	1.20	460	40.8	0.22	
CdTe/CdCl <sub>2</sub>	24.2	831	76.0	15.27	
CdSe <sub>x</sub> Te <sub>1-x</sub> /CdTe/CdCl <sub>2</sub>	28.3	854	75.8	18.30	

interdiffused CdTe absorber layer. It was observed that the strongest chlorine signal emanates from the CdTe grain boundary regions, with small Cl hotspots located in the interior of the grains. Figure 3b shows a plane-view image of the selenium signal intensity in the CdTe absorber. Apart from being concentrated at the CdTe grain boundaries, selenium signal is also present in the grain fringes. The superimposed image of the chlorine and selenium signals in Figure 3c further confirms that selenium diffuses into the CdTe grains while chlorine is mainly concentrated at the CdTe grain boundary regions. This suggests that during CdCl2 treatment of bilayer CdSeTe/CdTe absorbers, Se diffuses into the CdTe grains through the grain boundaries. While analyzing the Se-graded CdSeTe/CdTe absorber-based PV devices, Fiducia et al. and Guo et al. have made similar observations in different studies. 14,20 Figure 3e shows a line profile of the selenium and chlorine signals across two grain boundaries in the CdTe absorber layer. As described earlier, the selenium signal was found to be further diffused into the CdTe grain interior compared to chlorine (it should be noted that the chlorine profile will be widened due to the 50–100 nm spot size of the ion beam). Figure 3d shows 3D renderings of the selenium and chlorine signals, showing the diffusion of selenium into the CdTe grains.

Atomistic Modeling of the CdTe(110)/(100) Grain Boundary. After determining the Se and Cl distribution in the CdTe absorber film, the microstructural mapping of the CdTe film (different from NanoSIMS microscopy) at a random surface (schematic shown in Figure 4a) was performed with the electron backscatter diffraction (EBSD) technique. Figure 4b shows the inverse pole image of the CdCl<sub>2</sub>-treated CdTe film with different colors representing various grain orientations. As evident from Figure 4b, the CdTe grains orient themselves in random crystallographic directions forming distinct grain boundary regions. Since EBSD only gives 3 of the 5 macroscopic degrees of freedom that describe the grain boundary, the orientation of the grain boundary plane is random. Using the color code of CdTe grains, one random CdTe(110)/(100) grain boundary (see the zoomed view of Figure 4b) was chosen for the atomistic modeling. The basis for choosing the CdTe(110)/ (100) grain boundary also comes from the previous research study, where Sen et al. used DFT to analyze the electronic properties of the CdTe(110)/(100) grain boundary.<sup>21</sup> The atomistic CdTe(110)/(100) model represents an idealistic case of the grain boundary as the twist angle associated with the grain boundary is unknown.

Figure 4c shows the schematic of the two-probe CdTe(110)/ (100) grain boundary model (described in the Methods section). The interfacial energy per unit area,  $\gamma_{GB}$ , was calculated from DFT as follows<sup>22</sup>

$$\gamma_{\rm GB} = \frac{1}{2A} [E^{\rm total} - E_{\rm bulk,110} \times n_{110} - E_{\rm bulk,100} \times n_{100}]$$
 (1)

where  $E^{\text{total}}$  is defined as the total energy of the grain boundary model,  $E_{\rm bulk,110}$  and  $E_{\rm bulk,100}$  are the bulk total energies for (110) and (100) orientations, respectively,  $n_{110}$  and  $n_{100}$  are the repeating bulk equivalent unit cells in the respective (110) and (100) orientations that are required to form the central region of the two-probe model, and "A" is the cross-sectional area of the simulation domain. The calculated interfacial energy value came out to be  $1.37 \, \text{J/m}^2$  and is in good agreement with the published literature values.  $^{21,22}$ 

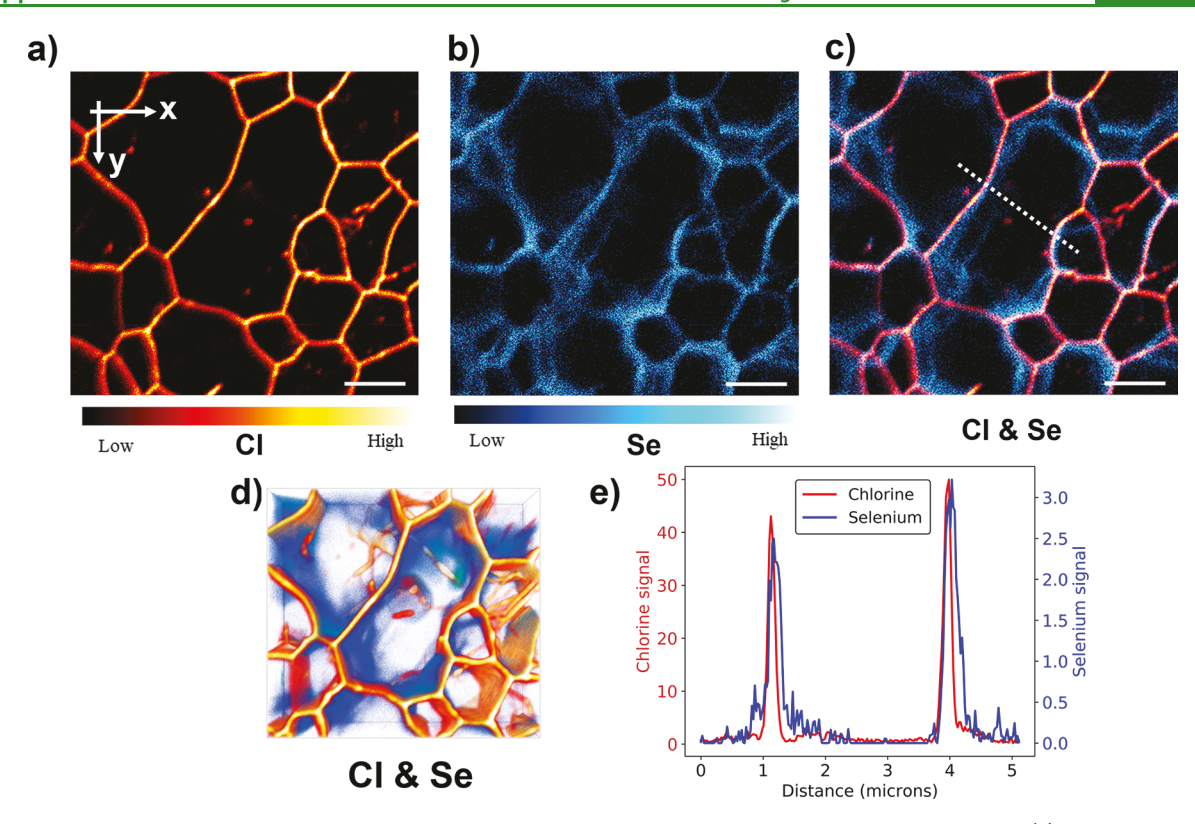


**Figure 3.** Planar NanoSIMS performed on the  $CdCl_2$ -treated CdSeTe/CdTe absorber, near the back contact, shows the (a) distribution of Cl along the CdTe grain boundaries, (b) distribution of Se along the CdTe grain boundaries, and (c) combined distribution of Cl and Se in the absorber. The white dotted line indicates the position of the line profile shown in (f). Scale bars for (a-c) are 2  $\mu$ m. (d) 3D rendering of the chlorine (shown in yellow and red color) and selenium (shown in blue color) distribution in the measurement volume. The x- and y-dimensions of the 3D renderings are 10 and 9.1  $\mu$ m, respectively. (e) Line profile of the Cl (red) and Se (blue) signal intensities across the region shown by the dashed line in (c).

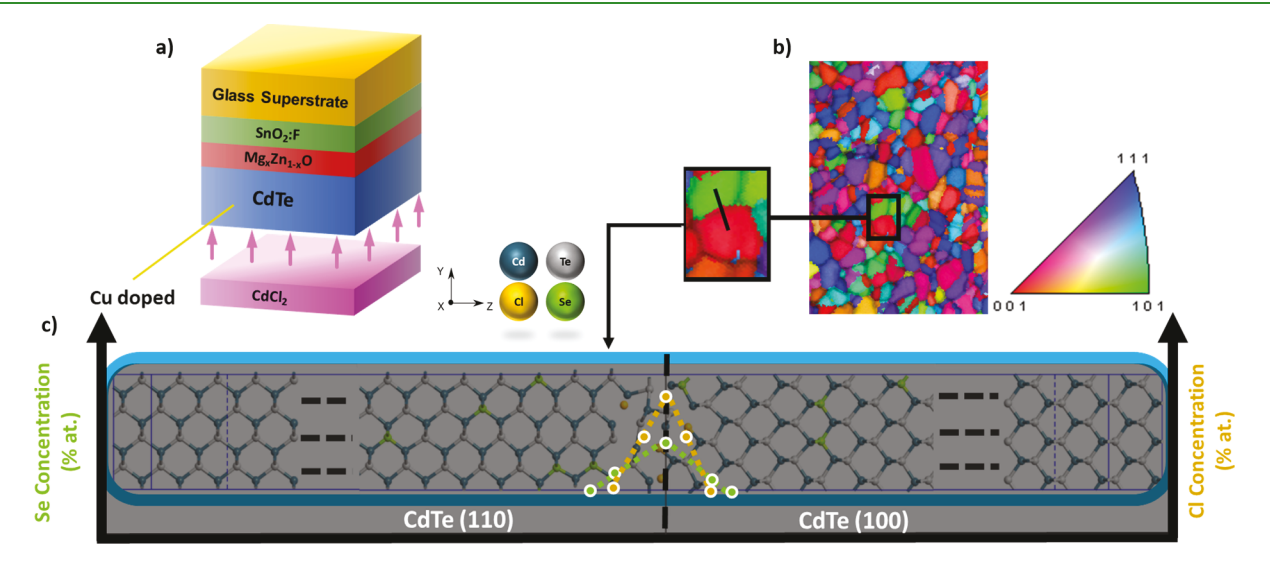


Figure 4. (a) Schematic of the  $CdCl_2$ -treated CdTe absorber film for surface EBSD analysis. (b) CdTe surface EBSD image showing various CdTe grain orientations and grain boundaries. The subfigure shows a zoomed view of the (110)/(100) CdTe grain boundary chosen for atomistic modeling. (c) Schematic showing a two-probe model of the CdTe (110)/(100) grain boundary. The dashed black line indicates the presence of the grain boundary. The gold and green lines show the respective Cl and Se atomic concentration distributed across the grain boundary (figure not drawn to scale). The modeled distribution is the first-order approximation of the experimental Se and Cl atomic concentration obtained from NanoSIMS analysis (Figure 3e).

For the Se- and Cl-alloyed CdTe grain boundaries, the interfacial energy  $\gamma_{\rm GB}$  using the two-probe model was found to be  $\sim -730 \, {\rm J/m^2}$ . While the energy was unreasonably lower than the typical grain boundary energy value, a negative sign would suggest that Cl and Se diffusion is favorable at the CdTe grain

boundary. The lower magnitude of the interfacial energy could be attributed to the current two-probe modeling setup, where the (110) and (110) repeating bulk unit cells constitute only of the Cd and Te atoms. Since Se and Cl atoms are missing from the bulk unit cell, the calculated energy values comes out to be

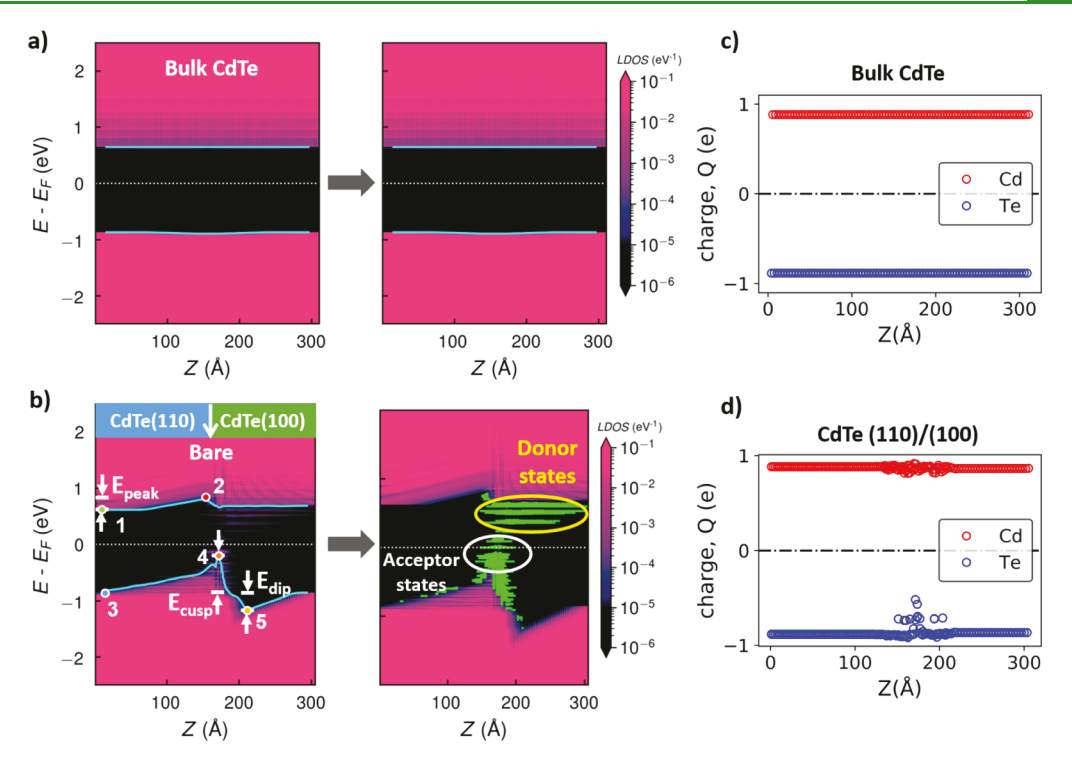


Figure 5. Energy band alignment diagram of the (a) bulk CdTe and (b) CdTe (110)/(100) grain boundary. The top arrow indicates the grain boundary plane. The white dotted line denotes the Fermi energy level, and the blue curves are the macroscopic average fits of the VBM and CBM. The second set of energy band alignment diagrams highlights the grain boundary defect states (indicated by green lines) mapped with respect to energy and localized positions based on the  $10^{-5}$ /eV local density of states (LDOS) cutoff value. Mulliken population analysis shows the atomic charge distribution for the (c) bulk CdTe and (d) CdTe (110)/(100) grain boundary.

much lower than expected energy values. Nonetheless, the interfacial energy for the Se + Cl-alloyed CdTe grain boundary still indicates that the segregation of Se and Cl atoms is favorable at the CdTe grain boundaries and can be verified from the NanoSIMS (see Figure 3) results and other published literature studies. <sup>12,14</sup>

It has been shown earlier by Li et al. that the CdCl<sub>2</sub> treatment of the CdTe absorber leads to substitution of chlorine in the tellurium sites. 12 Munshi et al., Fiducia et al., and Guo et al. have also reported that selenium from the CdSeTe layer grades into the CdTe absorber by substituting the tellurium sites. 1,13,14 Guo et al. using electron energy loss spectroscopy further analyzed a similar CdSeTe/CdTe device to arrive to the conclusion that  $\sim$ 35 at. % Cl and  $\sim$ 20 at. % Se substitutes the Te sites in the grain boundaries near the CdSeTe/CdTe interface. 14 Based on the atomic distribution of elemental Se and Cl atoms imaged through the NanoSIMS (Figure 3) technique and the literature reports described above, Se and Cl atoms were substituted randomly at the Te sites in the CdTe grain boundary atomistic model. In line with experimental observations, Figure 4c shows a first-order representation of the atomic distribution with the green dashed line representing the diffused Se atoms (maximum concentration ~20 at. %) and the gold dashed line representing the concentrated Cl atoms (maximum concentration ~35 at. %) in the two-probe CdTe(110)/(100) grain boundary model. However, it is to be noted here that unlike aberration-corrected transmission electron microscopy analysis, NanoSIMS imaging does not give the atomic configurations of the atoms at the grain boundaries. Therefore, as mentioned before, the current study utilized other literature reports for determining the Se and Cl atomic configurations in the two-probe atomistic models. 12,14

Pertinent electronic features of the CdTe(110)/(100)atomistic model were studied to understand the copassivation mechanism of alloying Se and Cl atoms in the CdTe grain boundaries. The energy band alignment plots for the bulk CdTe, bare CdTe grain boundary, and Se/Cl-alloyed CdTe grain boundary were generated by computing the local density of states and projecting them along the z-direction. Figures 5 and 6 show the energy band alignment diagrams with a macroscopically averaged curve fit of the valence band maximum (VBM) and conduction band minimum (CBM) calculated using the Gaussian kernel method described by Nicholson et al.<sup>23</sup> The band gap energies,  $E_{110}^g$  and  $E_{100}^g$ , were obtained from the energy differences of the CBM and VBM at positions located the closest to the bulk CdTe(110) and CdTe(100) electrode ends, respectively (Figure 6a). The energy band alignment diagram further shows various features such as a pickup/dip in the CBM and pickup/dip in the VBM. As per the labels provided in Figure 5b, the peak energy potential in the CBM,  $E_{\text{peak}}$  is defined as the energy difference between the peak curve fit of the CBM (labeled point 2) and the curve fit CBM value of the bulk-like CdTe(110) (labeled point 1). A positive value of  $E_{peak}$  indicates a pickup (barrier for electron charge carriers), while a negative value suggests a dip (enhancer for electron charge carriers) in the CBM at the CdTe(110)/(100) grain boundary. Similarly, cusp energy potential  $E_{\rm cusp}$  is defined as the energy difference between the peak value of the VBM (labeled point 4) and the VBM value of the bulk-like CdTe(110) (labeled point 3). The dip energy potential  $E_{\rm dip}$  is defined as the energy difference between the lowest dip value of the VBM (labeled point 5) and the VBM value of the CdTe(110) bulk-like region (labeled point 3). The presence of a dip in the VBM indicates an inversion from bulk p-type to n-type at the grain boundary and would act as a

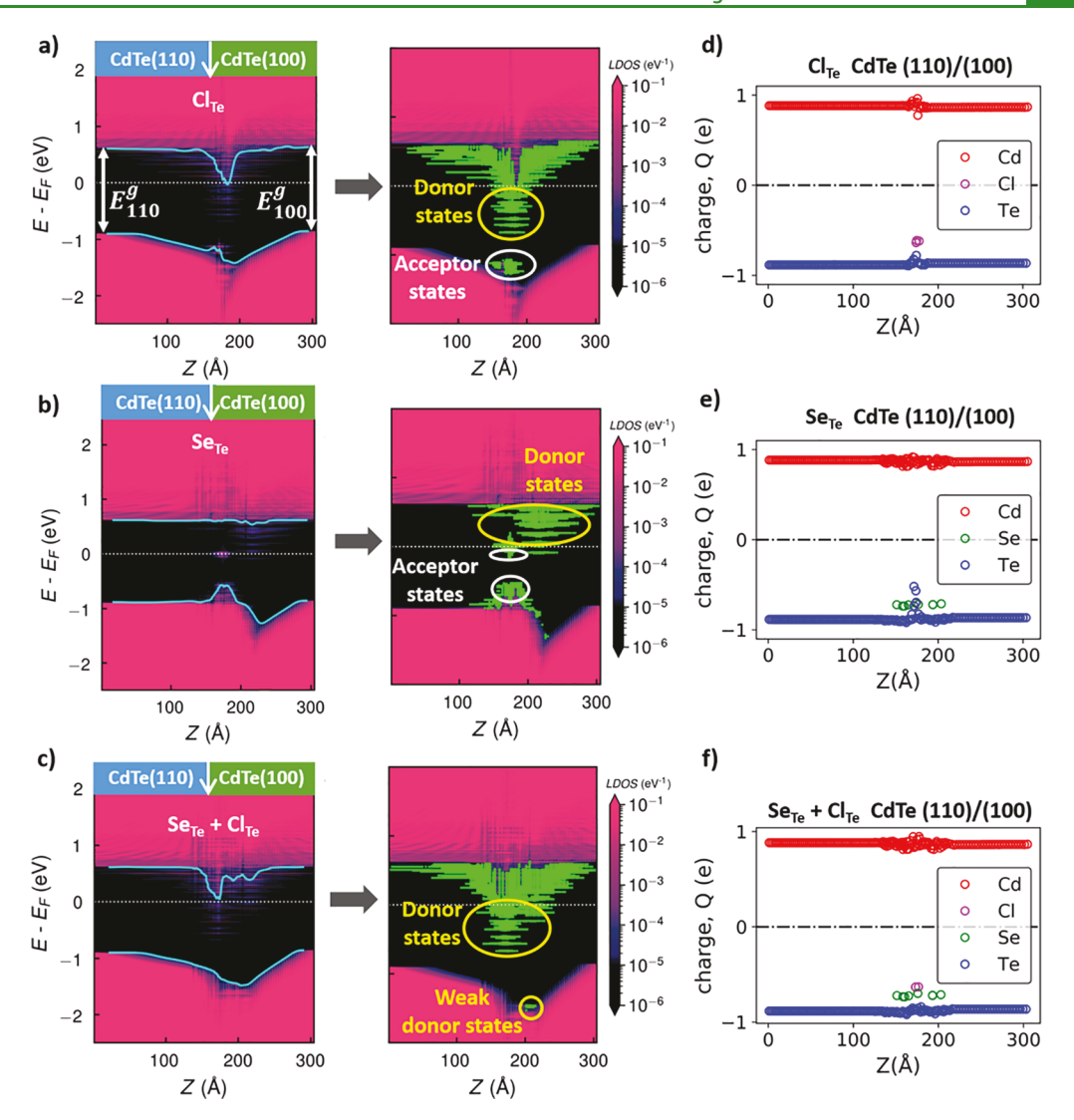


Figure 6. Energy band alignment diagram of the (a)  $Cl_{Te}$  CdTe (110)/(100) grain boundary, (b)  $Se_{Te}$  CdTe (110)/(100) grain boundary, and (c)  $Se_{Te}$  +  $Cl_{Te}$  CdTe (110)/(100) grain boundary along with their respective mapped defect states based on the  $10^{-5}$ /eV LDOS cutoff value. The top arrow indicates the grain boundary plane. Mulliken population analysis further shows the atomic charge distribution for the (d)  $Cl_{Te}$  CdTe (110)/(100) grain boundary, (e)  $Se_{Te}$  CdTe (110)/(100) grain boundary, and (f)  $Se_{Te}$  +  $Cl_{Te}$  CdTe (110)/(100) grain boundary.

barrier for the hole charge carrier transport across the grain boundary. Table 2 summarizes all the electronic features for

Table 2. Salient Electronic Features in the Energy Band Alignment of Various CdTe(110)/(100) Grain Boundaries

CdTe(110)/(100) grain boundary	$E_{110}^{\mathrm{g}}$ (eV)	$E_{100}^{\mathrm{g}}$ (eV)	$rac{E_{ m peak}}{({ m eV})}$	$\frac{E_{\mathrm{cusp}}}{(\mathrm{eV})}$	$\frac{E_{\mathrm{dip}}}{(\mathrm{eV})}$
bare	1.44	1.51	0.18	0.66	-0.33
$\mathrm{Cl}_{\mathrm{Te}}$	1.51	1.49	-0.64	_	-0.52
$Se_{Te}$	1.50	1.48	-0.05	0.30	-0.37
$Se_{Te} + Cl_{Te}$	1.51	1.48	-0.56	_	-0.58

various grain boundary cases described earlier. A small difference between the band gap values was observed for the bulk-like CdTe(110) and CdTe(100) regions. This difference is majorly due to the screening length which can be accommodated by increasing the number of atoms in the simulation. Nonetheless, the band gap values calculated with DFT-1/2 for the bulk-like CdTe ( $E_{110}^{g}$  and  $E_{100}^{g}$ ) far away from the grain boundary are in good agreement with the existing literature. <sup>22,23</sup>

Classification of the Defect States. Figure 5a,b shows the energy band alignment features of the bulk CdTe and bare CdTe(110)/(100) grain boundary, respectively. Figure 5c,d shows the partial charge distribution (obtained by a Mulliken population analysis  $^{24}$ ) on the Cd and Te atoms along the transverse z-direction for the respective bulk CdTe and CdTe(110)/(100) grain boundary models. Cationic behavior is indicated by a positive electronic charge, while anionic behavior is depicted by a negative electronic charge on the atoms. Figure 5c shows a smooth charge distribution for the bulk CdTe, as the anions and cations are arranged periodically with no perturbation in the electrostatic potential. This unperturbed electrostatic potential manifests itself into a defect state free flat energy band alignment diagram with an energy band gap value of  $\sim$ 1.51 eV throughout the bulk CdTe model.

However, the atoms at the CdTe(110)/(100) grain boundary deviate from the ordered anionic/cationic arrangement. The deviation from periodic arrangement of atoms induces a perturbation in the electrostatic potential and therefore affects the charges on the atoms (see Figure 5d) near the grain boundary region. Such a disordered arrangement of atoms with

varying degree of charge near the grain boundary creates electronic defect states in the band gap region. These defect states can be further classified into donor or acceptor states. A donor defect state is defined as the state which donates electrons to the CBM and in turn becomes positively charged while the acceptor states accept electrons from the VBM, thereby becoming negatively charged states. Figure 7 shows the density

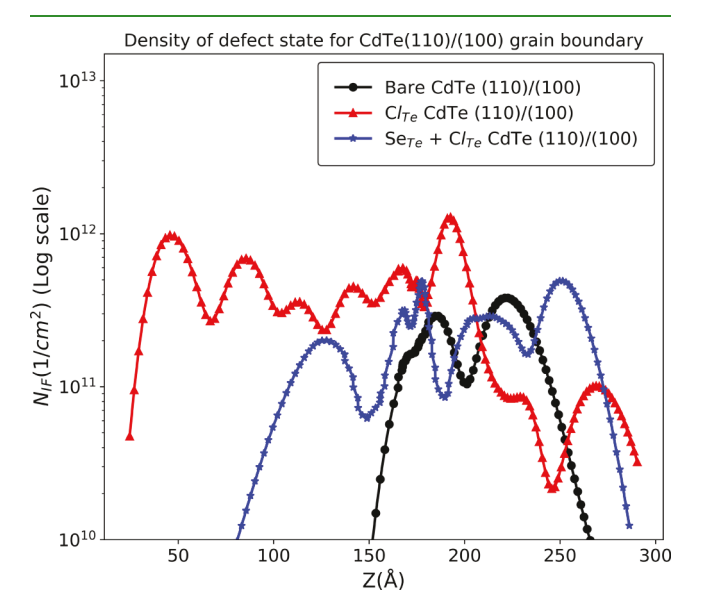


**Figure 7.** Density of the defect state with respect to the transverse *z*-direction for bare,  $Cl_{Te}$ -alloyed, and  $Se_{Te} + Cl_{Te}$ -alloyed CdTe (110)/ (100) grain boundary.

of defect states for the bare and alloyed CdTe(110)/(100) grain boundary cases. The quantified density of defect states is quantitatively in good agreement with other published literature studies. The presence of the defect states (shallow or deep levels) bends the bands depending on whether they are acceptor or donor defect states.

Therefore, it is important to understand the character of the defect states to comprehend the various electronic features observed in the energy band alignment diagram of bare/alloyed CdTe(110)/(100) grain boundaries. Based on the  $10^{-5}/eV$  LDOS cutoff value, the existing defect states (indicated by green

lines in Figure 5b) were algorithmically determined with respect to energy and localized positions (in the transverse z-direction) in the energy band alignment diagrams. Since the origin of these sub-band gap defect states is due to variation in the atomic charges, it was theorized that the characteristics of these defect states could be directly determined by summing the charges on the atoms contributing to the existence of these defect states. If the net charge on atoms contributing to a particular defect state was found to be positive/negative, that state would be classified as a donor/acceptor state.

In regard to this, clusters of the defect states existing near different energy band alignment features were identified and the ones having the highest LDOS value were analyzed to determine their respective character. For example, for the bare CdTe(110)/(100) grain boundary in Figure 5b, two groups of defect states near the  $E_{\rm cusp}$  and  $E_{\rm dip}$  energy potentials were identified. From the defect state group near the  $E_{\text{cusp}}$  energy potential, two defect states with the highest LDOS values at  $E_{\text{defect1}} = -0.118 \text{ eV (LDOS} = 0.17136 \text{ eV}^{-1}) \text{ and } E_{\text{defect2}} = 0 \text{ eV}$ (LDOS =  $0.02385 \text{ eV}^{-1}$ ) were selected for further analysis. Using the data generated after mapping the localized positions of the defect states,  $E_{\text{defect1}}$  extended from  $z_{\text{start}} = 144.11$  Å to  $z_{\text{end}} =$ 187.92 Å in the transverse z-direction. Using the Mulliken population plot in Figure 5d, it was found that a total of 74 atoms with a net -1.27 electronic charge was associated with  $E_{\text{defect1}}$ across the specified spatial range. Likewise, defect state 2 ( $E_{\text{defect}2}$ = 0 eV) was located from  $z_{\text{start}}$  = 148.80 Å to  $z_{\text{end}}$  = 196.21 Å with a total of 88 atoms having a net -1.26 electronic charge contributing to its existence. Since the net electronic charge on the atoms contributing to the defect state 1 and defect state 2 was negative, both of these defect states were classified as acceptor states.

Similarly, from the other group of defect states above the  $E_{\rm dip}$  energy potential, two defect states with the highest LDOS value at  $E_{\rm defect3}$  = 0.362 eV (LDOS = 0.05402 eV<sup>-1</sup>) and  $E_{\rm defect4}$  = 0.531 eV (LDOS = 0.69080 eV<sup>-1</sup>) were analyzed. Defect state 3 ( $E_{\rm defect3}$  = 0.362 eV) was located from  $z_{\rm start}$  = 155.83 Å to  $z_{\rm end}$  = 255.86 Å with a total of 180 atoms having a net +0.45 electronic charge. Likewise, defect state 4 ( $E_{\rm defect4}$  = 0.531 eV) was located from  $z_{\rm start}$  = 148.80 Å to  $z_{\rm end}$  = 298.94 Å with a total of 272 atoms having a net +1.33 electronic charge. Since the net electronic charge on the atoms contributing to the defect state 3 and defect

Table 3. Summary of the Analysis of Defect States for the Bare and Alloyed CdTe(110)/(100) Grain Boundary

alloy	$E_{\mathrm{defect}}$ (eV)	LDOS ( $eV^{-1}$ )	$z_{ m start}$ (Å)	$z_{ m end}$ (Å)	$N_{ m atoms}$	M.P. charge (e <sup>-</sup> )	defect State
	-0.118	0.17136	144.11	187.92	74	-1.270	acceptor
	0.000	0.02385	148.80	196.21	88	-1.260	acceptor
bare	+0.362	0.05402	155.83	255.86	180	+0.450	donor
	+0.531	0.69080	148.80	298.94	272	+1.330	donor
	-1.250	0.01599	167.82	187.69	25	-0.380	acceptor
	-1.230	0.12646	169.60	194.32	45	-0.400	acceptor
$Cl_{Te}$	-1.110	0.14756	146.46	191.00	80	-1.260	acceptor
	-0.293	0.32214	148.80	205.91	103	+1.320	donor
	-0.768	0.23196	137.16	205.32	120	-1.240	acceptor
	-0.056	0.03154	162.52	186.99	45	-2.210	acceptor
$Se_{Te}$	+0.037	0.21187	151.17	245.50	171	+1.380	donor
	+0.550	1.40320	185.32	262.07	140	+2.590	donor
	-1.460	0.00033	201.66	214.99	23	+0.009	weak donor
	-0.356	0.37712	141.76	202.98	108	+0.556	donor
$Se_{Te} + Cl_{Te}$	-0.068	0.01023	148.88	189.75	73	+1.410	donor
	+0.181	1.57267	137.16	228.24	164	+0.440	donor

state 4 was positive, these defect states were classified as donor states. Table 3 summarizes the analysis of various defect states for the bare CdTe(110)/(100) grain boundary. Based on the abovementioned analysis, it could be deduced that the cluster of defect states above the  $E_{\rm cusp}$  energy potential would be acceptor states (labeled with a white circle in Figure 5b) and the ones above the  $E_{\mathrm{dip}}$  energy potential would be donor states (labeled with a yellow circle in Figure 5b). Furthermore, these donor and acceptor states were classified as deep level defect states as they were found in the mid band gap region for the bare CdTe grain boundary model.

To understand the effect of alloying elements on the defect states, similar analyses were performed on the Se- and Cl-alloyed CdTe(110)/(100) grain boundary models. It was observed that the presence of Cl<sub>Te</sub> at the grain boundary leads to emergence of high density of deep level donor states (see Figure 6a) below the Fermi level. However, acceptor-type defect states were found near the VBM indicating the presence of shallow level acceptor states. This implies that passivating the grain boundaries with Cl<sub>Te</sub> eliminates the deep level acceptor defect states (found in the bare grain boundary) but introduces high density of deep level donor states.

The defect state analysis for the Se<sub>Te</sub>-alloyed CdTe grain boundary indicated a lower deep level acceptor state density (see Figure 6b) than the bare CdTe grain boundary case. In addition to this, the high density of both shallow and deep level donor states was found to exist above the Fermi level. However, alloying the grain boundary with Se<sub>Te</sub> + Cl<sub>Te</sub> revealed the exclusive presence of donor defect states. The model indicates that Se<sub>Te</sub> + Cl<sub>Te</sub> completely passivates the acceptor defects present in either of the bare, Cl<sub>Te</sub>-alloyed, or Se<sub>Te</sub>-alloyed CdTe grain boundaries (see Figure 6c). Table 3 summarizes the analysis of various defect states for the alloyed CdTe(110)/ (100) grain boundary.

It is also important to note here that this work does not attempt to relate the Mulliken population charge to the defect charge rather utilizes the Mulliken population charge to identify the nature of defect states. The Mulliken population charge on atoms consists of complex interactions between the electronic wave functions that forms defect states with different defect charge values. Therefore, establishing a relationship between the Mulliken population charge to the defect charge is complicated and is beyond the scope of the current work.

Effect of Defect States on the Energy Band Alignment **Diagram.** As described before, the presence of defect states has certain implications on the energy band alignment diagrams. The previous literature reports have shown that the high density of donor/acceptor states creates a dip/cusp energy potential in the VBM.<sup>25,26</sup> Similar effects were observed in the bare and alloyed CdTe grain boundaries. It was consistently found that the presence of donor defect states begins near the CBM and extends down toward the mid band gap region. This would facilitate the donation of minority electron charge carriers to the CBM by the donor states and would make them positively charged. The presence of positively charged donor defect states in the band gap region would further cause a repulsive field for hole charge carriers and create a barrier (dip energy potential) in the VBM. This further explains the existence of donor defect states above the  $E_{\rm dip}$  energy potential in the bare and alloyed CdTe grain boundaries (Figures 5 and 6).

Similarly, the acceptor states begin near the VBM and protrude into the band gap region. The shallower acceptor states would gain an electron from the VBM and create hole charge

carriers. This would generate an attractive electric field for the hole charge carriers and bends the VBM up toward the acceptor defect states leading to the formation of cusp electric potentials  $(E_{\text{cusp}})$  in the VBM. Such a trend was observed in all the grain boundary cases where acceptor states were found to exist above the VBM (see Figures 5b and 6b). For the Cl-alloyed CdTe grain boundary (Figure 6a), since the density of acceptor was not high, a small cusp-like feature in the VBM near the acceptor states was observed instead of a high energy cusp potential. This further confirms that, however small, the VBM always bends up in the vicinity of the acceptor states and bends down in the vicinity of the donor states. A similar conclusion is found for how donor/ acceptor states influencing the band-bending direction in the CBM. Such an approach to understand the impact of defect states on the energy band alignment behavior reinforces the Mulliken population analysis results that were used to characterize the defect states.

#### DISCUSSION

The atomistic modeling of the bare and alloyed CdTe(110)/ (100) grain boundary gives insights into the effect of the selenium and chlorine elements on the grain boundary electronic properties. The electronic properties of the bare, Cl<sub>Te</sub>-alloyed, and Se<sub>Te</sub> + Cl<sub>Te</sub>-alloyed CdTe grain boundary models could provide major insights into the performance of the untreated CdTe, CdCl2-treated CdTe, and CdCl2-treated CdSeTe/CdTe PV devices. It is a known fact that occupation probability of a defect state depends on its energy position  $(E_{def})$ relative to the Fermi level  $(E_t)$ . It has been shown previously that the occupation probability of a defect state  $(P(E_{def} - E_f))$  could be determined as<sup>26</sup>

$$P(E_{\text{def}} - E_{\text{f}}) = 1, \qquad E_{\text{def}} < E_{\text{f}} \tag{2}$$

$$P(E_{\text{def}} - E_f) = 0, \qquad E_{\text{def}} > E_f \tag{3}$$

In regard to the defect states, eqs 2 and 3 state that the donor(acceptor) state above(below) the Fermi level contains a positive(negative) charge.<sup>25</sup> As has been discussed before, for the bare CdTe grain boundary case (Figure 5b), the donor states above the Fermi level will be positively charged while the acceptor states will be negatively charged. Moreover, these states are in the close vicinity and therefore have a high probability of charge carrier recombination. Apart from that, a positive  $E_{\rm peak}$ value (see Table 2) in the CBM creates an electron reflectortype effect and  $E_{\text{dip}}$  (see Table 2) energy potential in the VBM creates a barrier for hole charge carriers. Therefore, the high probability of charge recombination at the grain boundary and transport barrier of the minority electron charge carriers (assuming a p-type CdTe absorber) at the grain boundary should limit the device performance of untreated CdTe solar

However, as described before, the Cl<sub>Te</sub> alloying of the CdTe grain boundary passivates the deep level acceptor states but induces high density of donor states. In one of the literature reports, Mhirech and Baddi showed that the existence of highdensity donor states leads to an inversion at the interface and is beneficial for extracting the minority charge carriers.<sup>26</sup> Similar effects were observed for the Cl<sub>Te</sub>-alloyed CdTe grain boundary in this study. The presence of high density of donor states leads to a negative  $E_{\rm peak}$  energy potential in the CBM and a high  $E_{\rm dip}$ energy potential in the VBM (see Table 2). This implies that both the CBM and VBM bend downward causing an n-type inversion (from a p-type grain interior) at the grain boundary. Due to this inversion, minority electron charge carriers would be attracted toward the grain boundary, while majority charge carriers would be repelled, leading to better charge carrier extraction. Moreover, the presence of shallower acceptor defect states further reduces the recombination in the  $\text{Cl}_{\text{Te}}$ -alloyed CdTe grain boundary. Such a low recombination and a better minority charge carrier collection in the  $\text{CdCl}_2$ -treated CdTe PV devices should improve the open-circuit voltage and short-circuit current density, as observed in Figure 2.

The  $Se_{Te} + Cl_{Te}$  alloying of the CdTe grain boundary passivates both the deep and shallow level acceptor states found in the respective bare and Cl<sub>Te</sub>-alloyed CdTe grain boundary. The high density of donor states maintains the inversion at the grain boundary, again allowing for a better minority electron charge carrier collection. This would further reduce the charge recombination (compared to the Cl<sub>Te</sub>-alloyed CdTe grain boundary) and increase the minority charge carrier lifetime for CdSeTe/CdTe PV devices. In the past, Guo et al. had made similar observations, where a minority carrier lifetime of 6.3 ns was measured for the  $Se_{Te}$  +  $Cl_{Te}$ -alloyed CdTe absorber in comparison with 1 ns lifetime obtained for the pure CdTe layer. 14 The low charge carrier recombination and improved minority charge carrier lifetime should further promote higher open-circuit voltages in CdCl2-treated CdSeTe/CdTe PV devices (see Figure 2a). The presence of the lower band gap CdSeTe material also leads to higher short-circuit current values (see Figure 2b), thereby improving the PV device efficiencies beyond 18%.

It is important to note that the overall efficiency improvements due to  $Se_{Te} + Cl_{Te}$  alloying of the CdTe absorber would also depend on the potentials created due to other grain boundary defects, grain size, interfaces created due to various front and back contacts, and bulk properties of the absorber. Li et al. in a previous study showed that the electrostatic field created due to the presence of Cl<sub>Te</sub> leads to n-type inversion and could be generalized for any random CdTe grain boundary. Although this is expected to hold true with respect to the energy band alignment results, a detailed systematic study is required to understand the passivating effect of  $Se_{Te} + Cl_{Te}$  atoms on the symmetric and random CdTe grain boundary orientation. Such an investigation using the methodologies presented in the current study would lead to a set of quantified defect parameters for various CdTe grain boundaries. These quantified defect parameters for diverse grain boundaries could be further utilized in 2D/3D device models to validate the experimental performance. Overall, the current study provides useful insights into the quantification and nature of the defect states, whose understanding could further enhance the performance of the CdTe solar cells.

# CONCLUSIONS

In summary, we compare the device performance parameters of the untreated CdTe, CdCl<sub>2</sub>-treated CdTe, and CdCl<sub>2</sub>-treated CdSeTe/CdTe PV devices. NanoSIMS characterization of highly efficient CdSeTe/CdTe devices reveals the elemental distribution of the selenium and chlorine atoms. While chlorine was found to be concentrated in the CdTe grain boundaries, selenium atoms were found to diffuse into CdTe grains via the grain boundary regions. The surface EBSD analysis of the CdTe film showed various grain orientations forming distinct grain boundary regions from which a random CdTe(110)/(100) grain boundary was chosen for the atomistic modeling. Various CdTe(110)/(100) grain boundary models including the bare,

 ${
m Cl_{Te}}$ -alloyed, and  ${
m Se_{Te}}+{
m Cl_{Te}}$ -alloyed CdTe grain boundary were simulated. The energy band alignment and the defect state properties evaluated using DFT calculations aid in deducing the mechanism for highly efficient CdSeTe/CdTe absorber-based PV devices. The presence of selenium- and chlorine-alloying atoms passivates the acceptor level defect states and induces high density of donor states. The passivation of acceptor defect states reduces the recombination, while the high-density donor states lead to n-type inversion at the grain boundary. The inversion from p-type grain interior to n-type grain boundary enhances the minority charge carrier collection, leading to a higher open-circuit voltage and short-circuit current density observed in highly efficient CdSeTe/CdTe PV devices.

# **■** METHODS

Cell Fabrication and NanoSIMS Characterization. PV devices with two CdTe and one CdSeTe/CdTe p-type absorbers were fabricated using an in-line sublimation system described by Swanson et al.  $^{27}$  A total of 20 small-area  $\sim\!0.65~{\rm cm}^2$  research devices were fabricated on NSG Pilkington TEC10 soda lime glass using the methods described by Munshi et al.  $^{1,2}$  The electrical measurements were performed after calibrating the current density and device area for each set of measurement to cells measured by National Renewable Energy Laboratory (NREL). For the NanoSIMS characterization, a region of the back surface of the absorber layer (i.e., in the CdTe part of the absorber, near the back contact) was first polished with a Xe ion beam to remove surface roughness and prepare the samples for SIMS measurements. NanoSIMS measurements were then performed on the polished region using the methods described by Fiducia et al.  $^{20}$ 

Computational Details. The CdTe(110)/(100) grain boundary model was simulated using the QuantumATK P-2019.03 software tool. The pseudopotential, basis sets and other modeling parameters for Cd, Se, Te, and Cl atoms were chosen from the earlier studies performed by Shah et al.  $^{15,22}$  All the simulations utilized the Perdew–Zunger form of local density approximation (LDA-1/2) $^{29}$  exchange correlation functional for the self-consistent calculations with  $6 \times 6 \times 150$  k-point sampling for CdTe grain boundary two-probe device simulations (schematic shown in Figure 4c).

# AUTHOR INFORMATION

#### Corresponding Author

Akash Shah — Department of Mechanical Engineering, Colorado State University, Fort Collins, Colorado 80523, United States; orcid.org/0000-0002-6108-4506; Email: akash.shah@colostate.edu

# **Authors**

Anthony P. Nicholson — Department of Mechanical Engineering, Colorado State University, Fort Collins, Colorado 80523, United States

Thomas A. M. Fiducia — CREST (Centre for Renewable Energy Systems Technology), Loughborough University, Loughborough, Leicestershire LE11 3TU, U.K.

Ali Abbas – CREST (Centre for Renewable Energy Systems Technology), Loughborough University, Loughborough, Leicestershire LE11 3TU, U.K.

Ramesh Pandey – Department of Physics, Colorado State
University, Fort Collins, Colorado 80523, United States

Junliang Liu – Department of Materials, University of Oxford, Oxford OX1 2JD, U.K.

Chris Grovenor – Department of Materials, University of Oxford, Oxford OX1 2JD, U.K.

John M. Walls — CREST (Centre for Renewable Energy Systems Technology), Loughborough University, Loughborough, Leicestershire LE11 3TU, U.K.

- Walajabad S. Sampath Department of Mechanical Engineering, Colorado State University, Fort Collins, Colorado 80523, United States
- Amit H. Munshi Department of Mechanical Engineering, Colorado State University, Fort Collins, Colorado 80523, United States

Complete contact information is available at: https://pubs.acs.org/10.1021/acsami.1c06587

#### **Notes**

The authors declare no competing financial interest.

This report was prepared as an account of work sponsored by an agency of the United States Government. Neither the United States Government nor any agency thereof, nor any of their employees, makes any warranty, express or implied, or assumes any legal liability or responsibility for the accuracy, completeness, or usefulness of any information, apparatus, product, or process disclosed, or represents that its use would not infringe privately owned rights. Reference herein to any specific commercial product, process, or service by trade name, trademark, manufacturer, or otherwise does not necessarily constitute or imply its endorsement, recommendation, or favoring by the United States Government or any agency thereof. The views and opinions of authors expressed herein do not necessarily state or reflect those of the United States Government or any agency thereof.

## ACKNOWLEDGMENTS

The material is partially based upon work supported by the U.S. Department of Energy's Office of Energy Efficiency and Renewable Energy (EERE) under Solar Energy Technologies Office (SETO) Agreement number DE-EE0008557 and DE-EE0008177. Acknowledgment goes out to the National Science Foundation Graduate Research Fellowship, INTERN, and NSF/IUCRC Programs for the support and funding of the current research work. This work utilized the Summit supercomputer, which is supported by the National Science Foundation (awards ACI-1532235 and ACI-1532236), the University of Colorado Boulder, and Colorado State University. J.L. and C.G. are grateful for support for the NanoSIMS facility from EPSRC under grant EP/M018237/1. All the material used in cell fabrication was supplied by 5N plus Inc.

### REFERENCES

- (1) Munshi, A. H.; Kephart, J.; Abbas, A.; Raguse, J.; Beaudry, J.-N.; Barth, K.; Sites, J.; Walls, J.; Sampath, W. Polycrystalline CdSeTe/CdTe Absorber Cells with 28 mA/cm2 Short-Circuit Current. *IEEE J. Photovoltaics* **2018**, *8*, 310–314.
- (2) Munshi, A. H.; Kephart, J. M.; Abbas, A.; Shimpi, T. M.; Barth, K. L.; Walls, J. M.; Sampath, W. S. Polycrystalline CdTe Photovoltaics with Efficiency Over 18% through Improved Absorber Passivation and Current Collection. *Sol. Energy Mater. Sol. Cells* **2018**, *176*, 9–18.
- (3) Kephart, J. M.; Kindvall, A.; Williams, D.; Kuciauskas, D.; Dippo, P.; Munshi, A.; Sampath, W. S. Sputter-Deposited Oxides for Interface Passivation of CdTe Photovoltaics. *IEEE J. Photovoltaics* **2018**, *8*, 587–593.
- (4) Hagenorf, C. Assessment of Performance, Environmental, Health and Safety Aspects of First Solar's CdTe Photovoltaic Technology, 2016.report
- (5) Bosio, A.; Romeo, N.; Podestà, A.; Mazzamuto, S.; Canevari, V. Why CuInGaSe2 and CdTe Polycrystalline Thin Film Solar Cells are More Efficient than the Corresponding Single Crystal? *Cryst. Res. Technol.* **2005**, *40*, 1048–1053.

- (6) Dharmadasa, I. Review of the CdCl2 Treatment Used in CdS/CdTe Thin Film Solar Cell Development and New Evidence towards Improved Understanding. *Coatings* **2014**, *4*, 282–307.
- (7) Paulson, P. D.; Dutta, V. Study of In Situ CdCl2 Treatment on CSS Deposited CdTe Films and CdS/CdTe Solar Cells. *Thin Solid Films* **2000**, 370, 299–306.
- (8) Schaffner, J.; Motzko, M.; Tueschen, A.; Swirschuk, A.; Schimper, H.-J.; Klein, A.; Modes, T.; Zywitzki, O.; Jaegermann, W. 12% Efficient CdTe/CdS Thin Film Solar Cells Deposited by Low-Temperature Close Space Sublimation. *J. Appl. Phys.* **2011**, *110*, 064508.
- (9) Kim, M.; Sohn, S.; Lee, S. Reaction Kinetics Study of CdTe Thin Films During CdCl2 Heat Treatment. Sol. Energy Mater. Sol. Cell. 2011, 95, 2295–2301.
- (10) Moutinho, H. R.; Al-Jassim, M. M.; Levi, D. H.; Dippo, P. C.; Kazmerski, L. L. Effects of CdCl2 Treatment on the Recrystallization and Electro-Optical Properties of CdTe Thin Films. *J. Vac. Sci. Technol., A* **1998**, *16*, 1251–1257.
- (11) Zhang, L.; Da Silva, J. L. F.; Li, J.; Yan, Y.; Gessert, T. A.; Wei, S.-H. Effect of Copassivation of Cl and Cu on CdTe Grain Boundaries. *Phys. Rev. Lett.* **2008**, *101*, 155501.
- (12) Li, C.; Wu, Y.; Poplawsky, J.; Pennycook, T. J.; Paudel, N.; Yin, W.; Haigh, S. J.; Oxley, M. P.; Lupini, A. R.; Al-Jassim, M.; Pennycook, S. J.; Yan, Y. Grain-Boundary-Enhanced Carrier Collection in CdTe Solar Cells. *Phys. Rev. Lett.* **2014**, *112*, 156103.
- (13) Fiducia, T. A. M.; Mendis, B. G.; Li, K.; Grovenor, C. R. M.; Munshi, A. H.; Barth, K.; Sampath, W. S.; Wright, L. D.; Abbas, A.; Bowers, J. W.; Walls, J. M. Understanding the Role of Selenium in Defect Passivation for Highly Efficient Selenium-Alloyed Cadmium Telluride Solar Cells. *Nat. Energy* **2019**, *4*, 504–511.
- (14) Guo, J.; Mannodi-Kanakkithodi, A.; Sen, F. G.; Schwenker, E.; Barnard, E. S.; Munshi, A.; Sampath, W.; Chan, M. K.; Klie, R. F. Effect of Selenium and Chlorine Copassivation in Polycrystalline CdSeTe Devices. *Appl. Phys. Lett.* **2019**, *115*, 153901.
- (15) Shah, A.; Munshi, A. H.; Nicholson, A. P.; Thiyagarajan, A.; Pozzoni, U. M.; Sampath, W. S. Atomistic Modeling of Energy Band Alignment in CdSeTe Surfaces. *Appl. Surf. Sci.* **2021**, *544*, 148762.
- (16) Watts, M. J.; Fiducia, T. A. M.; Sanyal, B.; Smith, R.; Walls, J. M.; Goddard, P. Enhancement of Photovoltaic Efficiency in CdSe x Te1-x (where 0 x 1): Insights from Density Functional Theory. *J. Phys.: Condens. Matter* **2019**, 32, 125702.
- (17) Wei, S.-H.; Zhang, S. B.; Zunger, A. First-Principles Calculation of Band Offsets, Optical Bowings, and Defects in CdS, CdSe, CdTe, and their Alloys. *J. Appl. Phys.* **2000**, *87*, 1304–1311.
- (18) Swanson, D. E.; Sites, J. R.; Sampath, W. S. Co-Sublimation of CdSexTe1x Layers for CdTe Solar Cells. *Sol. Energy Mater. Sol. Cells* **2017**, *159*, 389–394.
- (19) Kuciauskas, D.; Kephart, J. M.; Moseley, J.; Metzger, W. K.; Sampath, W. S.; Dippo, P. Recombination Velocity Less than 100cm/s at Polycrystalline Al2O3/CdSeTe Interfaces. *Appl. Phys. Lett.* **2018**, *112*, 263901.
- (20) Fiducia, T. A. M.; Li, K.; Munshi, A. H.; Barth, K.; Sampath, W. S.; Grovenor, C. R. M.; Walls, J. M. Three-Dimensional Imaging of Selenium and Chlorine Distributions in Highly Efficient Selenium-Graded Cadmium Telluride Solar Cells. *IEEE J. Photovoltaics* **2020**, *10*, 685–689.
- (21) Sen, F. G.; Buurma, C.; Paulauskas, T.; Sun, C.; Kim, M.; Sivananthan, S.; Klie, R. F.; Chan, M. K. Y. Atomistic Simulations of Grain Boundaries in CdTe. 2015 IEEE 42nd Photovoltaic Specialist Conference (PVSC), 2015; pp 1–5.
- (22) Shah, A.; Nicholson, A. P.; Thiyagarajan, A.; Sampath, W. S. First Principles Assisted Modeling to Understand Chlorine Passivation of CdTe Grain Boundary. 2020 47th IEEE Photovoltaic Specialists Conference (PVSC), 2020; pp 1760–1764.
- (23) Nicholson, A. P.; Martinez, U.; Shah, A.; Thiyagarajan, A.; Sampath, W. S. Atomistic Modeling of Energy Band Alignment in CdTe(1 0 0) and CdTe(1 1 1) Surfaces. *Appl. Surf. Sci.* **2020**, 528, 146832.
- (24) Mulliken, R. S. Electronic Population Analysis on LCAO. *J. Chem. Phys.* **1955**, 23, 1833.

- (25) Scheer, R.; Schock, H. W. Chalcogenide Photovoltaics; John Wiley Sons, Ltd, 2011; Chapter 2, pp 9–127.
- (26) Mhirech, A.; Baddi, M. Energy and the Environment; Pergamon: Oxford, 1990; pp 448–452.
- (27) Swanson, D. E.; Kephart, J. M.; Kobyakov, P. S.; Walters, K.; Cameron, K. C.; Barth, K. L.; Sampath, W. S.; Drayton, J.; Sites, J. R.; Kephart, J. M.; Kobyakov, P. S.; Walters, K.; Cameron, K. C.; Barth, K. L.; Sampath, W. S. Single Vacuum Chamber with Multiple Close Space Sublimation Sources to Fabricate CdTe Solar Cells. *J. Vac. Sci. Technol., A* **2016**, *34*, 021202.
- (28) QuantumATK 2019.03; Synopsys QuantumATK, 2019.
- (29) Ferreira, L. G.; Marques, M.; Teles, L. K. Approximation to Density Functional Theory for the Calculation of Band Gaps of Semiconductors. *Phys. Rev. B: Condens. Matter Mater. Phys.* **2008**, 78, 125116.
- (30) Perdew, J. P.; Ernzerhof, M.; Burke, K. Rationale for Mixing Exact Exchange with Density Functional Approximations. *J. Chem. Phys.* **1996**, *105*, 9982–9985.